

# On the detection of stellar differential rotation based on the Fourier transform of spectral line profiles

Yoichi TAKEDA<sup>1,2</sup>

<sup>1</sup>*National Astronomical Observatory, 2-21-1 Osawa, Mitaka, Tokyo 181-8588, Japan  
takeda.yoichi@nao.ac.jp*

<sup>2</sup>*SOKENDAI, The Graduate University for Advanced Studies, 2-21-1 Osawa, Mitaka, Tokyo 181-8588, Japan*

(Received 2019 May 28; accepted 2019 November 1)

## Abstract

It is known that stellar differential rotation can be detected by analyzing the Fourier transform of spectral line profiles, since the ratio of the first- and second-zero frequencies is a useful indicator. This approach essentially relies on the conventional formulation that the observed flux profile is expressible as a convolution of the rotational broadening function and the intrinsic profile, which implicitly assumes that the local intensity profile does not change over the disk. Although this postulation is unrealistic in the strict sense, how the result is affected by this approximation is still unclear. With an aim to examine this problem, flux profiles of several test lines (showing different center-to-limb variations) were simulated using a model atmosphere corresponding to a mid-F dwarf by integrating the intensity profiles for various combinations of  $v_e \sin i$  (projected rotational velocity),  $\alpha$  (differential degree), and  $i$  (inclination angle), and their Fourier transforms were computed to check whether the zeros are detected at the predicted positions or not. For this comparison purpose, a large grid of standard rotational broadening functions and their transforms/zeros were also calculated. It turned out that the situation critically depends on  $v_e \sin i$ : In case of  $v_e \sin i \gtrsim 20 \text{ km s}^{-1}$  where rotational broadening is predominant over other line broadening velocities (typically several  $\text{km s}^{-1}$ ), the first/second zeros of the transform are confirmed almost at the expected positions. In contrast, deviations begin to appear as  $v_e \sin i$  is lowered, and the zero features of the transform are totally different from the expectation at  $v_e \sin i$  as low as  $\sim 10 \text{ km s}^{-1}$ , which means that the classical formulation is no more valid. Accordingly, while the zero-frequency approach is safely applicable to studying differential rotation in the former broader-line case, it would be difficult to practice for the latter sharp-line case.

**Key words:** line: profiles – method: data analysis – stars: rotation – stars: solar-type

## 1. Introduction

It has been known since olden days (Huang 1961) that stellar differential rotation may be detected by analyzing the profiles of spectral lines. However, given the necessity of distinguishing very subtle difference of line shapes, early trials failed (Gray 1977, 1982) even by applying the Fourier transform technique, which is effective for extracting delicate information from line profiles (such as discrimination of rotation and turbulence; see, e.g., Gray 1988, 2005). It was at long last in the beginning this century when Reiners, Schmitt, and Kürster (2001) finally reported the existence of Sun-like differential rotation in  $\psi$  Cap (F5 dwarf) based on the canonical approach of comparing/fitting the transforms of observed and theoretical profiles for two blend-free lines (Fe I 5775 and Si I 5772) in the Fourier domain. Successively, Reiners and Schmitt (2002) found that the ratio of the frequencies at the first and second zeros in the Fourier transform of the broadening function is a good indicator of differential rotation, which provided a prospect of much easier model-independent detection by just measuring this ratio in the observed transform. Reiners and Schmitt (2003) further developed a method of extracting the rotational

broadening function ( $G$ ) from a spectrum of several tens Å portion by applying the Least Squares Deconvolution technique with the help of an appropriately adjusted template spectrum, by which the required first and second zeros can be effectively derived by transforming the resulting  $G$  of sufficiently high-S/N ratio. Since then, making use of these advantages, Reiners and his collaborators extensively examined the nature of differential rotation in A-, F, and G-type stars of slow as well as rapid rotators (see, e.g., Ammler-von Eiff & Reiners 2012, and the references therein).

Although their contributions in this field are regarded as significant, some concern still remains regarding the assumption upon which their analysis is founded. That is, their adopted methodology (use of the frequency ratios of first and second zeros in the Fourier domain, which are measured from the transform of the broadening function extracted by applying the deconvolution technique) is essentially based on the postulation that the observed flux spectrum  $F(\lambda)$ <sup>1</sup> is expressed by a convolution of the stellar

<sup>1</sup> For the case of line profile analysis, Fourier transform is usually applied to  $1 - F(\lambda)/F^{\text{cont}}$  (line depth relative to the local continuum) rather than  $F(\lambda)$  itself. Accordingly, it should be kept in mind that this meaning is implicitly contained in  $F(\lambda)$  used

unbroadened spectrum  $F_0(\lambda)$  and the rotational broadening function  $G(\lambda)$ :

$$F(\lambda) = F_0(\lambda) \otimes G(\lambda), \quad (1)$$

where  $\otimes$  means ‘‘convolution.’’ By Fourier transforming these quantities, such as

$$f(\sigma) \equiv \int_{-\infty}^{+\infty} F(\lambda) \exp(2\pi i \lambda \sigma) d\lambda, \quad (2)$$

we have

$$f(\sigma) = f_0(\sigma)g(\sigma), \quad (3)$$

which describes the advantage of Fourier technique; i.e., since ‘‘convolution’’ turns into simple ‘‘product’’ in the Fourier domain, the zeros of  $g(\sigma)$  are simply inherited to  $f(\sigma)$  to be directly observable.

It should be noted, however, that equation (1) is nothing but an assumption. Since observed flux is an integration of specific intensities over the stellar disk (whose spectra generally differ from position to position), the necessary condition for equation (1) to strictly hold is that  $I_0(\lambda)/I_0^{\text{cont}}$  (line shape of the residual intensity normalized by the continuum) does not vary over the disk; in this case, the residual flux  $F_0(\lambda)/F_0^{\text{cont}}$  can be equated to the position-independent  $I_0(\lambda)/I_0^{\text{cont}}$  (see, e.g., Gray 2005). Unfortunately, since this is an unrealistic condition (even the classical line-formation theory such as the Milne–Eddington model predicts a result against it; e.g., Eq. (10-29) in Mihalas 1978), characteristic center-to-limb variation in the strength/profile of any line must more or less exist.

Generally, in case of  $v_e \sin i$  (projected rotational velocity) determination, which is reflected by the line width (1st order effect), significant errors would not be expected even if equation (1) does not hold. However, detection of differential rotation ( $\alpha$ ) is a far more difficult and delicate task, which requires discriminating very subtle difference in the profile shape (2nd order effect). Thus, whether this assumption is valid or not may bring about crucial impact on the results of analysis, which should be clarified by all means.

Nevertheless, it has been barely investigated so far, to our knowledge, how much deviation from the profile constancy would be expected case by case or how much error would result by using equation (1) in the line-profile analysis. That is, investigators in this field have invoked this assumption without any convincing verification. Perhaps the main reason may be the insufficiency of information regarding how the profiles of different lines exhibit changes over the stellar disk.

In order to improve this situation, Takeda and UeNo (2017a, 2017b, 2019) recently conducted a comprehensive spectroscopic study to clarify the behaviors of the strengths and broadening widths across the solar disk for a number of spectral lines, and arrived at a reasonable understanding of their center-to-limb variations in terms of the line properties (e.g., species, excitation potential,

strength, etc.). It is, therefore, now possible to guess the tendency of center–limb variations of line profiles at least for solar-type stars.

Accordingly, the purpose of this study is to examine the validity of the method for detecting stellar differential rotation, which makes use of the zeros of Fourier transforms and is founded on the assumption of equation (1). This verification test consists of the following procedures:

- Model (flux) profiles of several representative test lines are simulated for various combinations of rotation parameters by integrating the intensity profiles at various points of the stellar disk, while taking into account the center–limb variations of local line profiles as well as continuum intensities (i.e., limb darkening).
- For each of the resulting flux profiles, Fourier transforms are computed, in which the positions of zero frequencies are then searched for. If the conventional assumption really holds, the first and second zeros ( $\sigma_1$  and  $\sigma_2$ ) should appear at the same positions as those given by  $g(\sigma)$  according to equation (3); in this case, the approach adopted by Reiners et al. is justified. Otherwise, the differential rotation judged by the  $\sigma_2/\sigma_1$  ratio can not be regarded as trustworthy any more.

In this way, this test would serve as a touchstone for the validity or applicability limit of the detection method of differential rotation by using  $\sigma_2/\sigma_1$ . As a prerequisite, however, it is necessary to know the precise positions of zeros in  $g(\sigma)$  (Fourier transform of the rotational broadening function  $G(\lambda)$ ) to be compared with the simulated ones, which is addressed first in the next section.

The remainder of this paper is organized as follows. Following section 2 (for the rotational broadening function), details of line-profile modeling are spelled out in section 3, where the selected 8 test lines, adopted angle-dependent micro/macro-turbulence, and simulations of line profiles as well as their Fourier transforms are described. Discussions of the results (limb-darkening coefficients, behaviors of zero frequencies, interpretation of previous studies, and how to deal with the slow-rotator case) are presented in section 4, which is followed by section 5 (summary and conclusion). In addition, two supplementary appendices are presented: Appendix 1 describes the behaviors of solar macro- and micro-turbulence based on the results of Takeda and UeNo (2019), which serve as the basis of the functional forms of the turbulences adopted in this study. Appendix 2 shows the results of test calculations, which demonstrate the significant impact of angle-dependence in turbulent velocities on the main conclusion.

## 2. Rotational broadening function

Regarding the rotational broadening function  $G$  to be used in equation (1), it can be evaluated only numerically when a star rotates differentially (unlike the case of rigid rotation where  $G$  is analytically expressible). Although this was tried by several earlier studies in 1980s

(Bruning 1981, 1982; García-Alegre, Vázquez, & Wöhl 1982), Reiners and Schmitt (2002) computed this function more extensively for various combinations of the parameters. However, since these previous investigations employed a simple method of integrating the profile of a test line over the stellar disk (by Doppler shifting according to the local line-of-sight velocity), such computed  $G$  is not exact but more or less approximate, because the test line can not be a  $\delta$ -function but has a finite width. In this study is adopted an alternative method of using iso-velocity contours (cf. Huang 1961), by which precise evaluation of  $G$  is possible.

Let two coordinate systems having the common origin and common  $x, x'$ -axis be defined,  $(x, y, z)$  and  $(x', y', z')$ , where the  $y$ -axis of the former is the line of sight and the  $z'$ -axis of the latter is the rotation axis of a star, both making an inclination angle  $i$  (cf. figure 1). As usually done, the rotation law of a (spherical) star is assumed to be

$$\omega(l) = \omega_e(1 - \alpha \sin^2 l), \quad (4)$$

where  $\omega$  is the angular velocity at a latitude  $l$ ,  $\omega_e$  is the equatorial angular velocity, and  $\alpha$  is the parameter indicating the degree of differential rotation.<sup>2</sup> Then, in the  $(x', y', z')$  system, the line-of-sight velocity of a stellar surface element as viewed along the  $y'$  direction is written as

$$v_{y'} = x' \omega_e (1 - \alpha z'^2), \quad (5)$$

where the position coordinates are expressed in unit of the stellar radius. Further, measuring the velocity in unit of the equatorial rotation velocity by introducing the non-dimensional parameter  $k$  ( $\equiv v/v_e$ ) this equation reduces to

$$k' = x' (1 - \alpha z'^2). \quad (6)$$

In the  $(x, y, z)$  system, this relation is transformed as

$$k = x [1 - \alpha (-\sqrt{1 - x^2 - z^2} \cos i + z \sin i)^2], \quad (7)$$

which defines the iso-velocity trajectory  $c_k(x, z)$  on the  $x$ - $z$  plane corresponding to any given velocity  $k$  ( $-1 \leq k \leq 1$ ).<sup>3</sup>

<sup>2</sup> This form is widely used in most stellar applications, which was devised in analogy with the solar differential rotation. In the solar case, however, the  $\sin^4 l$  term is often included in addition to the  $\sin^2 l$  term (see, e.g., Sect. 4.2 of Takeda & Ueno 2011)

<sup>3</sup> For the purpose of determining iso-velocity contours, it is not necessarily practical to directly use this equation (7), because  $x$  can not be described by an analytical function of  $z$ ,  $\alpha$ , and  $i$  (though  $z$  is expressed analytically in terms of  $x$ ,  $\alpha$ , and  $i$ ). It is much easier to start from equation (6), which defines a closed “loop” of iso-velocity on the stellar sphere, in the sense that all surface points on this loop (symmetric with respect to the  $x'$ - $z'$  plane) have the same line-of-sight velocity as seen along the  $y'$ -direction. Here, the bottom line is that this 3-dimensional loop on the sphere retains its iso-velocity character also in the  $(x, y, z)$  system (i.e., as seen along the  $y$ -direction). Then, what should be done is just to transform the  $(x', y', z')$  coordinates of all the points on this loop into the  $(x, y, z)$  system. The resulting  $(x, z)$  coordinates simply provide for the iso-velocity contour, though it has to be kept in mind that the points with  $y > 0$  should not be included (because they are on the invisible side of the sphere).

Some examples of  $c_k(x, z)$  contours for selected representative cases ( $\alpha = -0.4, 0.0, +0.4$  and  $i = 10, 50, 90^\circ$ ) are depicted in figure 2. Then,  $G(k)$  (rotational broadening function at  $k$ ) is calculated by integrating the visible area of iso-velocity band (whose width is proportional to  $(\partial k / \partial x)^{-1}$ ; i.e., breadth in  $x$  per unit  $k$ ) while taking into account the limb-darkening effect (assumed to follow the linear law)

$$I(\theta) = I_0(1 - \epsilon + \epsilon \cos \theta), \quad (8)$$

where  $\epsilon$  is the limb-darkening coefficient,  $I_0$  is the intensity at the disk center, and  $\theta$  is the angle of the outgoing ray relative to the surface normal. That is,

$$G(k) \propto \int_{c_k(x, z)} (\partial k / \partial x)^{-1} (1 - \epsilon + \epsilon \sqrt{1 - x^2 - z^2}) dz, \quad (9)$$

where the integration is carried out along the contour  $c_k(x, z)$  corresponding to  $k$ .

The computations of  $G(k)$  (for 201 points from  $k = 0$  to 1 with an increment of 0.005) were done for 4158 cases with combinations of 21 values of  $\alpha$  ( $-5.0, -4.5, -4.0, \dots, +4.5, +5.0$ ), 18 values of  $i$  ( $5^\circ, 10^\circ, 15^\circ, \dots, 85^\circ, 90^\circ$ ), and 11 values of  $\epsilon$  ( $0.0, 0.1, 0.2, \dots, 0.9, 1.0$ ). The resulting data of these broadening functions  $G(k)$  are presented as online materials (each of the “gprofs\_a????e??? .dat” files). Then, their Fourier transforms  $g(q)$ <sup>4</sup> were then computed, and the zero frequencies as well as the heights of sidelobes were further measured, as summarized in the online data table “g\_transform\_info.dat”.

It may be worth comparing the resulting values of the key quantities known as indicators of differential rotation, such as  $q_2/q_1$  (second-to-first zero frequency ratio) or  $I_1/I_2$  (first-to-second sidelobe height ratio), with those derived by Reiners and Schmitt (2002). Such a comparison is illustrated in figures 3a–3d, which are confirmed to be reasonably consistent with Fig. 5 and Fig. 7 of their paper. Likewise, figures 3e and 3f show that  $\alpha/\sqrt{\sin i}$  can be approximated by analytical functions of  $q_2/q_1$ , as argued by Reiners and Schmitt (2003) [cf. their Fig. 11 along with their equations (5) and (6)].

### 3. Modeling of spectral line profiles

#### 3.1. Assumed stellar parameters

Since Reiners and his colleagues have investigated the nature of differential rotation mainly for stars around F-type (i.e., late-A through early-G dwarfs), this study focuses on a F5 dwarf as a representative example, for which the following stellar parameters may be assigned by consulting Table B.1 of Gray (2005).  $T_{\text{eff}} = 6500$  K (effective temperature),  $M = 1.4 M_\odot$  (stellar mass),  $R = 1.4 R_\odot$  (stellar radius),  $\log g = 4.29$  (surface gravity in cgs unit, derived from  $M$  and  $R$ ), and  $[\text{Fe}/\text{H}] = 0.0$  (solar metallicity). The model atmosphere used for this study was

<sup>4</sup> In this study, non-dimensional Fourier frequency (corresponding to the non-dimensional variable  $k$  in the real space) is denoted as  $q$ , distinguished from the frequency  $\sigma$  used in equation (2) which has the dimension of wavelength<sup>-1</sup>.

generated by interpolating Kurucz's (1993) ATLAS9 grid of solar metallicity models.

### 3.2. Center-to-limb variations of solar spectral lines

Since the line profiles of an F5 star are to be simulated in the solar analogy, the center–limb variations in the line strengths/widths over the solar disk should make an important basis, for which the consequences of Takeda and UeNo (2017a, 2017b, 2019) are briefly summarized below.

- Regarding the macroturbulence, the frequently used radial-tangential model was concluded to be inadequate, while the classical Gaussian model being more preferable. The solar Gaussian macroturbulence ( $v_{\text{mac}}$ ) moderately increases toward the limb from  $\sim 1\text{--}2\text{ km s}^{-1}$  (center) to  $\sim 2\text{--}3\text{ km s}^{-1}$  (limb), though some dependence upon the line strength is also observed (cf. Fig. 9 in Takeda & UeNo 2017a, where this macroturbulence is denoted as  $V_{\text{los}}$ ). See also figure 9 in appendix 1.
- The trends of center-to-limb variations in the equivalent widths are diversified case by case (mainly depending upon the temperature sensitivity), which are classified in terms of (a) whether the species is of minor population or major population (determined by the ionization potential), (b) excitation potential, and (c) line strength (i.e., saturation degree) (Takeda & UeNo 2017b, 2019).
- The logarithmic change of the equivalent width ( $W$ ) relative to the disk center value ( $W_0$ ) is in the range of  $|\log(W/W_0)| \lesssim 0.3$ , whichever a line is strengthened or weakened toward the limb (Takeda & UeNo 2017b, 2019).
- An angle-dependent microturbulence ( $v_{\text{mic}}$ ) (i.e., increasing toward the limb) has to be introduced (except for unsaturated very weak lines), in order to reproduce such established trend of center–limb variation in  $W$ , which can be concluded by analyzing Takeda and UeNo's (2019)  $W$  data (such as done by Holweger, Gehlsen, & Ruland 1978). See also figure 10 in appendix 1.

### 3.3. Choice of turbulence parameters

By consulting the case for the Sun summarized in the previous subsection, the  $v_{\text{mac}}$  and  $v_{\text{mic}}$  to be used for an F5 star were assigned as follows, while postulating that (i) solar values are scaled by taking into account the differences of atmospheric parameters and (ii) similar angle-dependence (i.e., functional form of  $\theta$ ) holds.

The empirical formula for  $v_{\text{mic}}$  of F–G stars derived by Takeda et al. (2013; cf. equations (1) and (2) therein) yields  $v_{\text{mic}} = 1.07\text{ km s}^{-1}$  (Sun;  $T_{\text{eff}} = 5780\text{ K}$ ,  $\log g = 4.44$ ) and  $v_{\text{mic}} = 1.76\text{ km s}^{-1}$  (F5 dwarf;  $T_{\text{eff}} = 6500\text{ K}$ ,  $\log g = 4.29$ ). Accordingly, the scaling relation of  $v^{\text{F5}}/v^{\odot} \simeq 1.6$  is assumed for both  $v_{\text{mac}}$  and  $v_{\text{mic}}$ . Although this scaling factor was derived from the  $v_{\text{mic}}$  vs.  $T_{\text{eff}}$  relation, it is almost consistent with the similar trend for  $v_{\text{mac}}$ . Regarding the graphical overview of the published  $T_{\text{eff}}$ -dependent relations, see Fig. 7 (left panel) of Ryabchikova et al. (2016)

and Fig. 1d of Takeda, Hashimoto, and Honda (2017) for  $v_{\text{mic}}$ , while Fig. 7 (right panel) of Ryabchikova et al. (2016) and Fig. 14 of Takeda and UeNo (2017a) for  $v_{\text{mac}}$ .

By examining the results of  $v_{\text{mac}}$  (Gaussian macroturbulence) derived by Takeda and UeNo (2017a) for the Sun,  $v_{\text{mac}}^{\odot}$  may be roughly approximated by the relation<sup>5</sup>

$$v_{\text{mac}}^{\odot}(\theta) = 1.5 + 1.0\sin\theta \quad (\text{km s}^{-1}), \quad (10)$$

which further yields

$$v_{\text{mac}}^{\text{F5}}(\theta) = 2.4 + 1.6\sin\theta \quad (\text{km s}^{-1}) \quad (11)$$

by applying the scaling relation.

Regarding the solar microturbulence  $v_{\text{mic}}^{\odot}$ , Holweger, Gehlsen, and Ruland (1978) derived  $1.0\text{ km s}^{-1}$  (disk center) and  $1.6\text{ km s}^{-1}$  (near to the limb at  $\cos\theta = 0.3$  or  $\sin\theta = 0.95$ ). Then, by assuming the angle-dependence similar to that of macroturbulence, we may write

$$v_{\text{mic}}^{\odot}(\theta) = 1.0 + 0.6\sin\theta \quad (\text{km s}^{-1}), \quad (12)$$

which is further scaled as

$$v_{\text{mic}}^{\text{F5}}(\theta) = 1.6 + 1.0\sin\theta \quad (\text{km s}^{-1}). \quad (13)$$

The center-to-limb behaviors of the finally adopted macro- and micro-turbulences for the F5 star,  $v_{\text{mac}}^{\text{F5}}(\theta)$  and  $v_{\text{mic}}^{\text{F5}}(\theta)$  expressed by equations (11) and (13), are graphically shown in figure 4a.

### 3.4. Adopted test lines

As mentioned in subsection 3.2, the center-to-limb variations of equivalent widths differ from line to line depending on the line properties. After some trial calculations, 8 fictitious lines (Fe I lines of  $\chi_{\text{low}} = 0, 3, \text{ and } 6\text{ eV}$ ; O I line of  $\chi_{\text{low}} = 9\text{ eV}$ ; two kinds of line strengths for each case with  $W_0 = 30\text{ m}\text{\AA}$  and  $100\text{ m}\text{\AA}$ ; line center wavelength at  $5000\text{ \AA}$ ) were decided to adopt (cf. table 1), which were so selected as to reproduce such a diversified center–limb variations in the range of  $|\log(W/W_0)| \lesssim 0.3$  as shown by the Sun. The resulting  $W(\theta)$  values for each line, which were computed by Kurucz's (1993) WIDTH9 program with the angle-dependent microturbulence  $v_{\text{mic}}^{\text{F5}}(\theta)$  [cf. equation (13)], are plotted against  $\cos\theta$  in figure 4b. In addition, the  $W$  vs.  $\cos\theta$  trends corresponding to a constant (i.e., angle-independent)  $v_{\text{mic}}$  of  $1.6\text{ km s}^{-1}$  are also depicted in figure 4c for comparison (which are related to the test calculations described in appendix 2).

### 3.5. Line profile calculation

For the purpose of simulating line profiles of a differentially rotating star, the modified version of the program code CALSPEC (Takeda, Kawanomoto, & Ohishi 2008) was used, which generates the stellar flux spectrum by integrating the specific intensities along the line of sight at each of the many small segments over the visible disk (computed with the corresponding  $v_{\text{mic}}$  from the model atmosphere and then broadened according to the relevant  $v_{\text{mac}}$ ). Since only comparatively slow rotators are involved

<sup>5</sup> It turned out that the use of  $\sin\theta$  is better (than using  $\cos\theta$ ), if the  $\theta$ -dependence is to be represented by such a simple linear-term relation.

in this study, gravity darkening as well as gravity distortion were neglected, which means that the star's shape remains spherical, the continuum intensity (dependent only on  $\theta$ ) is always circularly symmetric on the disk, and only one atmospheric model of  $(T_{\text{eff}}, \log g) = (6500, 4.29)$  is relevant.

Regarding the three parameters ( $v_e \sin i$ ,  $\alpha$ , and  $i$ ) to be specified for simulating a line profile, calculations were done for combinations of 5 values of  $v_e \sin i$  (10, 20, 30, 40, and 50 km s<sup>-1</sup>), 11 values of  $\alpha$  (-0.5, -0.4, -0.3, ..., +0.4, +0.5), and 9 values of  $i$  (10°, 20°, 30°, ..., 80°, 90°). The profiles of 8 lines (table 1) were computed for all these cases in the wavelength range of [4998 Å, 5002 Å] with an increment of 0.005 Å (i.e., 801 points within  $\pm 2$  Å from the line center).

Then, the Fourier transforms were computed for the line depths  $[1 - F(\lambda)/F^{\text{cont}}]$  of the resulting profiles, and the positions of zero frequencies ( $\sigma_1, \sigma_2, \dots$ ) were measured. Since these  $\sigma$ 's have dimensions of wavelength<sup>-1</sup>, they were transformed into non-dimensional frequencies ( $q_1, q_2, \dots$ ) by the relation

$$q_j = \sigma_j \lambda (v_e \sin i) / c \quad (j = 1, 2, \dots) \quad (14)$$

( $\lambda$ : wavelength,  $c$ : speed of light), which are independent of  $v_e \sin i$  and directly comparable with  $q$ 's of the broadening function  $G(k)$  derived in section 2.

## 4. Discussion

### 4.1. Limb-darkening coefficient

As a preparation for comparing the Fourier transform properties (i.e., zero frequencies) of simulated line flux profiles (computed by integrating the local model-based intensity profiles over the disk) with those of the rotational broadening function  $[G(k; i, \alpha, \epsilon)]$ , it is necessary to adequately specify the value of  $\epsilon$  (limb-darkening coefficient) compatible with the calculated model profiles. Although in the papers of Reiners group (e.g., Ammler-von Eiff & Reiners 2012) was varied this parameter between 0 and 1 (around the standard value of 0.6) to estimate the uncertainty range of  $q_2/q_1$  as if it was unknown, its value relevant for the atmospheric parameters (especially  $T_{\text{eff}}$ ) and line wavelength adopted in this study was evaluated from the model atmosphere. Figures 5a–5c show the spectral distribution (of the specific intensity  $I_\nu$  at the disk center computed by ATLAS9 program),  $I_\nu$  vs.  $\cos\theta$  relations (along with the linear-regression lines) at representative wavelengths, and the resulting  $\epsilon$  values plotted against wavelength, respectively. In the present case where the wavelengths of fictitious lines were assumed to be 5000 Å, figure 5c indicates that  $\epsilon = 0.6$  is a reasonable choice.

### 4.2. Behaviors of zero positions

Figure 6 demonstrates how the zero frequencies ( $q_1, q_2$ , and  $q_3$ ) measured from the transforms of the simulated profiles (cf. subsection 3.5), which were computed for the 2600c30w100 case with 3 values of  $v_e \sin i$  (10, 20, and

30 km s<sup>-1</sup>),<sup>6</sup> 5 values of  $\alpha$  (-0.4, -0.2, 0.0, +0.2, and +0.4), and 9 values of  $i$  (10°, 20°, ..., and 90°), are compared with those corresponding to the standard rotational broadening function for  $\epsilon = 0.6$  (cf. section 2). Although this figure is for the 2600c03w100 case, the situations for the other 7 lines (cf. table 1) are almost similar and not much different.

It is apparent from figure 6 that whether the consistency is realized or not critically depends upon  $v_e \sin i$ :

— For the case of  $v_e \sin i = 30$  km s<sup>-1</sup> (right panels), a satisfactory agreement is observed for any of  $q_1, q_2$ , and  $q_3$ , except for the low  $i$  ( $< 50^\circ$ ) cases at  $\alpha = +0.4$ , where the transform  $g(q)$  has problems in terms of zero detection (cf. the caption to figures 3).

— However, regarding the  $v_e \sin i = 20$  km s<sup>-1</sup> case (center panels), an appreciable deviation begins to appear in  $q_3$  (especially for larger  $\alpha$  values) though  $q_1$  and  $q_2$  are still in agreement.

— Finally at the  $v_e \sin i = 10$  km s<sup>-1</sup> case (left panels), any consistency vanishes in the sense that the predicted zeros are not reproduced at all by the transforms of simulated transforms.

Regarding the  $q_2/q_1$  ratio, which has been used as a useful indicator of differential rotation (cf. section 1), the relative differences of  $(q_2/q_1)_{\text{mes}}$  (measured from the transform of simulated profiles) and  $(q_2/q_1)_{\text{exp}}$  (expected from  $g(q)$ ) are plotted against  $(q_2/q_1)_{\text{exp}}$  in figure 7 for each of the 8 lines. This figure confirms that the tendency described above (i.e., the critical role of  $v_e \sin i$ ) similarly holds for all the studied lines irrespective of the differences in center-to-limb variations. It is also worth noting that the discrepancy is more likely to be seen for larger (positive)  $\alpha$  in the transition case. For example, in the center and right panels ( $v_e \sin i = 20$  and 30 km s<sup>-1</sup>) of figure 7, the results for  $\alpha = +0.4$  (represented by filled squares at lower  $(q_2/q_1)_{\text{exp}}$  of  $\sim 1.2$ –1.4) show more deviations compared to the cases of other (smaller)  $\alpha$ .

Consequently, the following conclusion may be drawn regarding the applicability of Fourier transform method for spectroscopically detecting stellar differential rotation.

- In the realistic case where line-profiles are not constant over the disk, the validity of equation (1) depends upon the extent of  $v_e \sin i$  in comparison to the other broadening velocities (thermal velocity,  $v_{\text{mic}}$ , and  $v_{\text{mac}}$ ; root-mean-square is  $\sim 5$  km s<sup>-1</sup> in the present case).
- If the former is predominant over the latter (i.e.,  $v_e \sin i \gtrsim 30$  km s<sup>-1</sup>), equation (1) is practically valid and the  $q_2/q_1$  ratios expected from the rotational broadening function are reproduced in the transforms of actual profiles.
- However, if the latter is comparable (or not negligible) to the former (i.e.,  $v_e \sin i \lesssim 20$  km s<sup>-1</sup>),

<sup>6</sup> Although the actual calculations were done for five values of  $v_e \sin i$  (10, 20, 30, 40, and 50 km s<sup>-1</sup>), only the first three cases are discussed in this paper, because the results for 40 and 50 km s<sup>-1</sup> turned out to show a similar tendency as that for 30 km s<sup>-1</sup>.

even a small deviation from the constancy can violate the expected zeros in the transform and thus equation (1) does not hold any more.

- In addition, around the critical  $v_e \sin i$  ( $\sim 20 \text{ km s}^{-1}$ ), the risk for the breakdown of equation (1) tends to be higher as  $\alpha$  increases.

In a different perspective, an intuitive and qualitative interpretation of these trends may be possible. That is, the classical method is applicable if the line profile shows a characteristic shape of rotational broadening function (i.e., rounded **U** shape), which yields conspicuous sidelobes and clear zeros in the Fourier space. On the other hand, if the profile has lost such a rotational shape to have a rather sharp appearance (i.e., **V** shape such as like a Gaussian function), zeros as well as sidelobes are hardly detected in the Fourier space, which means that the procedure invoking zero frequencies does not have any chance. Accordingly, if thermal/turbulent velocities are no more negligible compared to  $v_e \sin i$ , Fourier transform method using  $q_2/q_1$  would become ineffective because line profiles tend to have an undesirable **V** shape. Likewise, in the transition case of critical  $v_e \sin i$  ( $\sim 20 \text{ km s}^{-1}$ ), the same goes if  $\alpha$  is sufficiently large (which makes profiles sharper; cf. Fig. 3 in Reiners & Schmitt 2002).

#### 4.3. Impact on the results of previous studies

In a number of papers published by Reiners and his collaborators was investigated the nature of differential rotation for various A-, F-, and G-type stars of a wide range of stellar rotation ( $v_e \sin i$  from a few  $\text{km s}^{-1}$  to  $\sim 300 \text{ km s}^{-1}$ ; see, e.g., Ammler-von Eiff & Reiners 2012) by using the  $q_2/q_1$  ratio. It may be appropriate here to review the consequences established by them based on what has been elucidated in this study.

According to the conclusion described in subsection 4.2, their results would have no problems as long as stars showing moderate or large rotational broadening ( $v_e \sin i \gtrsim 20\text{--}30 \text{ km s}^{-1}$ ) are concerned (which constitute most of their sample stars), because the observed  $q_2/q_1$  ratio can be regarded as equivalent to that of the standard rotational broadening function (reflecting the degree of differential rotation). Therefore, their first detection of differential rotation ( $\alpha \simeq 0.15$ ) for  $\psi$  Cap based on the Fourier transforms of Fe I 5775 or Si I 5772 line profiles (cf. Reiners, Schmitt, & Kürster 2001; Reiners & Schmitt 2002) should be all right, since this star is sufficiently broad-lined ( $v_e \sin i = 42 \text{ km s}^{-1}$ ).

However, the situation is different for slow rotators ( $v_e \sin i \lesssim 10\text{--}20 \text{ km s}^{-1}$ ), where the  $q_2/q_1$  ratio is no more usable because the zero frequencies in the Fourier space considerably deviate from the positions expected from the broadening function (or even zeros do not appear at all). This means that differential rotation can not be studied by this technique any more for such sharp-lined stars.<sup>7</sup>

<sup>7</sup> What matters here is Reiners et al.’s comparatively later results related to low  $v_e \sin i$  stars, which were based on the broadening function ( $G$ ) derived by applying the LSD technique to spectra of wide wavelength coverage (i.e., not from individual line pro-

In this context, it may be worth remarking that Reiners et al. also mentioned the applicability limit of their method concerning  $v_e \sin i$ , in the sense that a critical value of (minimum)  $v_e \sin i$  exists, below which their Fourier transform method using zero frequency ratio is no more effective. However, what is meant by the  $v_e \sin i$  limit in their papers simply concerns the spectral resolution<sup>8</sup> (sampling step) of line profile data, on which Fourier transform is calculated. That is, since the relevant zero frequencies ( $\sigma_1$  and  $\sigma_2$ ; containing information of rotation) progressively shift to higher frequency range as  $v_e \sin i$  decreases,  $\sigma_2$  is no more measurable once it exceeds the Nyquist frequency ( $\sigma_N$ ; determined by the sampling step) because of the aliasing problem, by which the limiting value of minimum  $v_e \sin i$  is defined. For example, Reiners and Schmitt (2003; see Sect. 3 therein) states that “To detect differential rotation on stars with  $v_e \sin i < 20 \text{ km s}^{-1}$ , spectra with a resolution of  $R \geq 100000$  are needed” (see also Fig. 9 in Reiners & Schmitt 2002). In contrast, the consequence of this study is essentially different, which implies “intrinsic” inapplicability of the  $\sigma_2/\sigma_1$  method for slow rotators of  $v_e \sin i < 20 \text{ km s}^{-1}$  (regardless of the sampling step or spectrum resolving power).

#### 4.4. Prospect of line profile study for slow rotators

Then, how could the information of rotational features for low  $v_e \sin i$  stars ( $\lesssim 10 \text{ km s}^{-1}$ ) be extracted from

files) as mentioned in section 1. In the author’s opinion, the consequence of this study specifically derived for single-line profile analysis equally applies to the wide-range spectrum analysis with the LSD method for the following reasons: (i) Since the proposition that “equation (1) is no longer valid for such slow rotators” was proved for all 8 representative lines chosen to cover the various center–limb variations of most lines, it should apply to any spectral lines (or their aggregates). (ii) This means that the breakdown of equation (1) at low  $v_e \sin i$  is expected also for wide-range spectra comprising many lines in general. (iii) As such, any results obtained by LSD for slow rotators should not be reliable, because equation (1) is the fundamental postulation of LSD (i.e., deconvolution). In this respect, their important conclusion, such as that the fraction of solar-like differential rotators ( $\alpha > 0$ ) tends to progressively increase with a decrease in  $v_e \sin i$  (amounting to  $\sim 60\%$  at  $v_e \sin i \sim 10\text{--}20 \text{ km s}^{-1}$ ; cf. Fig. 8 in Ammler-von Eiff & Reiners 2012), should be regarded with caution and worth reinvestigation. However, an anonymous referee of this paper objected to this view, arguing that (a) information derived for only 8 fictitious lines does not suffice to discuss the results obtained by LSD method because many lines of diverse properties are involved and (b) extensive calculation of realistic theoretical synthetic spectrum including a large number of lines and its inverse analysis by the LSD technique (just like Reiners et al. did) is necessary. Since such large-scale simulation is outside the scope of this paper, the author would take modest attitude of not concluding anything about the validity of Reiners et al.’s results obtained by LSD for the moment, the clarification of which by future studies is awaited.

<sup>8</sup> It appears that the term “spectral resolution” (denoted by  $R$ ) is used in their papers to represent  $\lambda/\Delta x$  (e.g., Reiners & Schmitt 2002), where  $\Delta x$  is the sampling step (in the same unit as the wavelength  $\lambda$ ), by which the Nyquist frequency is defined as  $\sigma_N \equiv 1/(2\Delta x)$ . Accordingly, the difference from the usual meaning of  $R \equiv \lambda/\Delta\lambda_{\text{FWHM}}$  should be kept in mind, where  $\Delta\lambda_{\text{FWHM}}$  is the full-width at half-maximum of the instrumental profile (the relation  $\Delta\lambda_{\text{FWHM}} \sim 2\text{--}3 \Delta x$  typically holds in the normal use of the spectrograph).

their line profiles? Since equation (1) does not hold and the information of rotational broadening function is useless in this case, a universally applicable simple approach (such as the use of only  $q_2/q_1$ ) should not be counted upon any more. Presumably, there is no royal road but to carefully compare the observed profile with the theoretical ones simulated by the disk integration method (such as done in this study).

As a demonstration, the line profiles ( $F(\lambda)/F^{\text{cont}}$ ) and their Fourier transform amplitudes ( $|r(q)|$ ) of the 2600c30w100 line computed for the  $v_e \sin i = 10 \text{ km s}^{-1}$  case are illustrated in figure 8. It can be seen from this figure (right-hand panels) that the appearance of  $r(q)$  considerably changes by varying  $\alpha$  as well as  $i$ , which means that studying Fourier transforms is still useful for separate determinations of these parameters (even though the predictions from the broadening function are useless here). Besides, the line flux profile itself would also be helpful, though its variations are generally subtle. For example, the residual flux at  $\lambda \simeq 5000.1 \text{ \AA}$  ( $F(\lambda)/F^{\text{cont}} \sim 0.7$ ) is a “fixed point” (i.e., invariable for changing  $i$  or  $\alpha$ ), as seen from the left-hand panels of figure 8, which may be used to establish  $v_e \sin i$  without prior knowledge of  $\alpha$  and  $i$ . Consequently, careful analysis of line profiles in both the wavelength and Fourier space, combined by extensive theoretical simulations, may open the way to clarifying the rotational properties of sharp-line stars, though this would be a much more difficult task compared to the case of broad-line stars.

## 5. Summary and conclusion

The nature of differential rotation in A-, F-, and G-type stars has been extensively investigated by Reiners et al. by making use of the fact that the ratio of the first- and second-zero frequencies ( $q_2/q_1$ ) in the Fourier transform of spectral line profiles is a useful indicator.

However, their approach relies on the conventional formulation that the observed flux profile is expressed as a convolution of the rotational broadening function and the intrinsic profile (cf. equation(1)), which implicitly assumes that the local intensity profile does not change over the disk. Although this postulation of profile constancy is unrealistic in the strict sense, how the result is affected by this approximation has barely been investigated so far.

In order to examine the validity of this assumption, flux profiles were simulated for eight fictitious lines (showing different center-to-limb variations) for various combinations of  $v_e \sin i$ ,  $\alpha$ , and  $i$ , while integrating the intensity profiles at many points on the visible disk calculated by using a model atmosphere corresponding to a mid-F dwarf along with adequately specified angle-dependent  $v_{\text{mac}}(\theta)$  and  $v_{\text{mic}}(\theta)$ . Fourier transforms of these profiles were further computed in order to check whether the zeros are detected at the positions predicted by the rotational broadening function.

For this purpose, a large grid of standard rotational broadening functions (for various combinations of  $\alpha$ ,  $i$ , and  $\epsilon$ ) were calculated in advance by using the iso-velocity

contours, and the zero frequencies were measured from their Fourier transforms. These data are presented as on-line materials.

The check revealed that the situation critically depends on the extent of  $v_e \sin i$ . In case of  $v_e \sin i \gtrsim 20 \text{ km s}^{-1}$  where rotational broadening is predominant over other broadening velocities (several  $\text{km s}^{-1}$ ), the first/second zeros of the transform are detected almost at the expected positions. In contrast, deviations begin to appear as  $v_e \sin i$  is lowered, and the zero features of the transform are totally different from the expectation at  $v_e \sin i$  as low as  $\sim 10 \text{ km s}^{-1}$ , which means that the classical formulation is not valid any more. In summary, while zero-frequency approach is safely applicable to studying differential rotation in the former broader-line case, it would be difficult to practice for the latter sharp-line case.

## Appendix 1. Anisotropy of macro- and micro-turbulences in the solar photosphere

The heart of this investigation is to simulate the profiles of various lines at different disk points of an F5 dwarf as realistic as possible. For this purpose, the solar center-limb variation data in the strengths as well as widths of many spectral lines recent published by Takeda and UeNo (2019) were consulted for reference, since we may reasonably postulate that the qualitative characteristics of the surface properties are not much different for F5 and G2 dwarfs.

As usually done in stellar spectroscopy, a very rough modeling was exploited for the solar photospheric velocity fields (affecting line profiles), which are divided into “micro”-turbulence ( $v_{\text{mic}}$ ) and “macro”-turbulence ( $v_{\text{mac}}$ ) and separately treated, where the former (microscopic scale) is included in the Doppler with of the line-opacity profile (like thermal velocity) while the latter (macroscopic scale) acts as a global velocity distribution function (like rotational broadening function) to be convolved with the intrinsic profile. Although this dichotomous model characterized by two parameters ( $v_{\text{mic}}$  and  $v_{\text{mac}}$ ) is known to be far from realistic (especially compared with the recent state-of-the-art 3D time-dependent hydrodynamical modeling), it is very useful in the practical sense because the widths and strengths of any spectral lines can be reasonably modeled if these fudge parameters are appropriately adjusted.

It has been known that angle-dependence has to be introduced to both  $v_{\text{mic}}$  and  $v_{\text{mac}}$  in order to reproduce the observed solar center-limb variations of spectral line strengths/widths, as occasionally reported by previous investigators; e.g., Holweger, Gehlsen, and Ruland (1978) for the microturbulence, or Gurtovenko (1976; cf. Fig. 2 therein) for the macroturbulence (non-thermal velocity dispersion). Actually, the same argument could be made based on the data compiled by Takeda and UeNo (2019), which eventually lead to the use of equation (10) (for  $v_{\text{mac}}^{\circ}$ ) and equation (12) (for  $v_{\text{mic}}^{\circ}$ ) adopted in subsection 3.3. Since the use of such anisotropic  $v_{\text{mic}}$  or  $v_{\text{mac}}$  is essentially important for the conclusion of this study (cf. ap-

pendix 2), some additional explanations are presented regarding the validity of these relations.

Figure 9 depicts how the  $v_{\text{mac}}^9$  values depend upon the mean formation depth ( $\log \tau$ ) and the view angle ( $\sin \theta$ ), which were derived by Takeda and UeNo (2019) at each point of the solar disk for 280 Fe I lines, Figures 9e–h manifestly show that  $v_{\text{mac}}$  progressively increases toward the limb and its  $\theta$ -dependence can be well represented by equation (10) on the average. Since it appears difficult to attribute this tendency solely to the depth-dependence as was occasionally argued in the old studies, some kind of real anisotropy should exist in the macroscopic turbulent velocity dispersion.

Regarding  $v_{\text{mic}}$ , it is known to significantly affect the strengths of stronger saturated lines (on the flat part of the curve of growth) but not those of weak lines (on the linear part of the curve of growth). In figures 10a–e are plotted the abundance differences relative to the disk-center value against  $\cos \theta$ , which were derived for 280 Fe I lines based on  $W$  values published by Takeda and UeNo (2019) by assuming  $v_{\text{mic}} = 1 \text{ km s}^{-1}$ . It can be seen from these figures that (although the consistency is almost accomplished for weak lines) the abundance discrepancy for stronger lines progressively increases towards the limb, which indicates that the observed center–limb trends of stronger lines can not be reproduced by a constant microturbulence and thus an angle-dependent  $v_{\text{mic}}$  increasing toward the limb is necessary to achieve consistency (i.e., position-independent abundances). Actually, figure 10f reveals that the systematic discrepancy can be considerably mitigated by using the  $\theta$ -dependent  $v_{\text{mic}}$  given by equation (12).

## Appendix 2. Importance of the angle-dependence of turbulent velocities

With an aim to simulate the profiles of various lines at different disk points of an F5 dwarf as realistic as possible, this study adopted special  $\theta$ -dependent anisotropic forms for both  $v_{\text{mic}}$  and  $v_{\text{mac}}$  expressed by equations (11) and (13) as described in subsection 3.3, which were devised in analogy with the solar case by making use of Takeda and UeNo’s (2019) recent study (cf. appendix 1). However, it may be more common for most people to simply assign constant values to these fudge parameters for modeling line profiles if information is lacking. In this respect, it would be instructive to examine how the conclusions derived in subsection 4.2 are affected if constant (angle-independent) values are used for  $v_{\text{mic}}$  or  $v_{\text{mac}}$ .

For this purpose, additional test calculations were carried out for the following three cases with different treatments of  $v_{\text{mic}}$  and  $v_{\text{mac}}$ : Case 1 ...  $v_{\text{mic}} = 1.6 \text{ km s}^{-1}$  (constant) while  $v_{\text{mac}}(\theta)$  unchanged. Case 2 ...  $v_{\text{mic}}(\theta)$  unchanged while  $v_{\text{mac}} = 2.4 \text{ km s}^{-1}$  (constant). Case 3 ...  $v_{\text{mic}} = 1.6 \text{ km s}^{-1}$  (constant) and  $v_{\text{mac}} = 2.4 \text{ km s}^{-1}$  (constant). The resulting behaviors of  $q_2/q_1$  corresponding to  $v_e \sin i = 10 \text{ km s}^{-1}$  are illustrated in figure 11 (left, middle,

and right panels correspond to Cases 1, 2, and 3, respectively), which are so arranged as to be directly comparable with the left-hand panels in figure 7 ( $v_e \sin i = 10 \text{ km s}^{-1}$  case, where the measured ratios are in marked conflict with the expected value from the broadening function). The following characteristics are read by inspecting figure 11 in comparison with figure 7.

- Case 1 results (left panels in figure 11) indicate that changing only  $v_{\text{mic}}$  (while  $v_{\text{mac}}$  still  $\theta$ -dependent) does not have any essential impact, While this is naturally expected for weak lines ( $W_{\mu=1} = 30 \text{ m\AA}$ ; lower 4 panels) which are anyhow insensitive to  $v_{\text{mic}}$ , the situation is not much improved even for  $v_{\text{mic}}$ -sensitive stronger lines ( $W_{\mu=1} = 100 \text{ m\AA}$ ; upper 4 panels) either.
- However, the results of Case 2 (middle panels in figure 11) reveal that adopting a constant  $v_{\text{mac}}$  (while  $v_{\text{mic}}$  still  $\theta$ -dependent) yields a remarkable improvement (i.e., recovery of expected  $q_2/q_1$  ratios) for three weak lines (2600c00w030, 2600c30w030, 2600c60w030), though the other remaining lines still show appreciable discrepancy.
- Interestingly, expected  $q_2/q_1$  ratios are much better (though not perfectly) reproduced for all of the 8 lines in Case 3 (right panels in figure 11) where constant values are used for both  $v_{\text{mic}}$  ( $1.6 \text{ km s}^{-1}$ ) and  $v_{\text{mac}}$  ( $2.4 \text{ km s}^{-1}$ ), which means that application of equation (1) is not necessarily bad even at  $v_e \sin i$  as low as  $\sim 10 \text{ km s}^{-1}$  (i.e., in marked contrast to the conclusion of this study).
- Consequently, realistic treatment (i.e., inclusion of  $\theta$ -dependence) for  $v_{\text{mic}}$  as well as  $v_{\text{mac}}$  is essentially important, because simply adopting constant values for these parameters yields incorrect results. This argument applies more significantly to  $v_{\text{mac}}$  (controlling widths of all lines) than to  $v_{\text{mic}}$  (affecting the strengths of stronger lines).

## References

- Ammler-von Eiff, M., & Reiners, A. 2012, *A&A*, 542, A116  
 Bruning, D. H. 1981, *ApJ*, 248, 274  
 Bruning, D. H. 1982, *A&A*, 115, 203  
 García-Alegre, M. C., Vázquez, M., & Wöhl, H. 1982, *A&A*, 106, 261  
 Gray, D. F. 1977, *ApJ*, 211, 198  
 Gray, D. F. 1982, *ApJ*, 258, 201  
 Gray, D. F. 1988, *Lectures on Spectral-Line Analysis: F, G, and K stars* (Arva, Ontario, The Publisher)  
 Gray, D. F. 2005, *The Observation and Analysis of Stellar Photospheres*, 3rd ed. (Cambridge, Cambridge University Press)  
 Gurtovenko, E. A. 1976, *Sov. Astron.*, 19, 488  
 Holweger, H., Gehlsen, M., & Ruland, F. 1978, *A&A*, 70, 537  
 Huang, S.-S. 1961, *ApJ*, 133, 130  
 Kurucz, R. L. 1993, *Kurucz CD-ROM*, No. 13 (Harvard-Smithsonian Center for Astrophysics)  
 Mihalas, D. 1978, *Stellar Atmospheres*, 2nd ed. (San Francisco, W. H. Freeman and Company)  
 Reiners, A., & Schmitt, J. H. M. M. 2002, *A&A*, 384, 155

<sup>9</sup> Note that this parameter was denoted as  $V_{\text{los}}$  in Takeda and UeNo (2019).

- Reiners, A., & Schmitt, J. H. M. M, 2003, A&A, 398, 647  
 Reiners, A., Schmitt, J. H. M. M., & Kürster, M. 2001, A&A, 376, L13  
 Ryabchikova, T., et al. 2016, MNRAS, 456, 1221  
 Takeda, Y., Hashimoto, O., & Honda, S. 2017, PASJ, 69, 1  
 Takeda, Y., Honda, S., Ohnishi, T., Ohkubo, M, Hirata, R., & Sadakane, K. 2013, PASJ, 65, 53  
 Takeda, Y., Kawanomoto, S., & Ohishi, N. 2008, ApJ, 678, 446  
 Takeda, Y., & Ueno, S. 2011, Solar Phys., 270, 447  
 Takeda, Y., & UeNo, S. 2017a, PASJ, 69, 46  
 Takeda, Y., & UeNo, S. 2017b, Solar Phys., 292, 123  
 Takeda, Y., & UeNo, S. 2019, Solar Phys., 294, 63

**Table 1.** Fictitious test lines used for the simulation.

Code (1)	$\lambda$ (2)	Species (3)	$\chi_{\text{low}}$ (4)	$\log \epsilon gf$ (5)	$W_0$ (6)	$W_{\text{limb}}$ (7)
2600c00w100	5000	Fe I	0.0	3.98	100	118
2600c30w100	5000	Fe I	3.0	6.64	100	102
2600c60w100	5000	Fe I	6.0	8.91	100	74
0800c90w100	5000	O I	9.0	8.78	100	51
2600c00w030	5000	Fe I	0.0	2.64	30	48
2600c30w030	5000	Fe I	3.0	5.25	30	37
2600c60w030	5000	Fe I	6.0	7.72	30	25
0800c90w030	5000	O I	9.0	7.58	30	11

(1) Line code. (2) Wavelength (in  $\text{\AA}$ ). (3) Element species. (4) Lower excitation potential (in eV). (5) Logarithm of the product of adopted oscillator strength ( $gf$ ) and elemental abundance ( $\epsilon$ ) which was so adjusted as to reproduce the specified equivalent width at the disk center, where  $\log \epsilon$  is defined as  $\log(N_X/N_H) + 12$  as usual. (6) Equivalent width (in m $\text{\AA}$ ) at the disk center ( $\mu = \cos \theta = 1.0$ ). (7) Equivalent width (in m $\text{\AA}$ ) at the limb ( $\mu = \cos \theta = 0.1$ ).

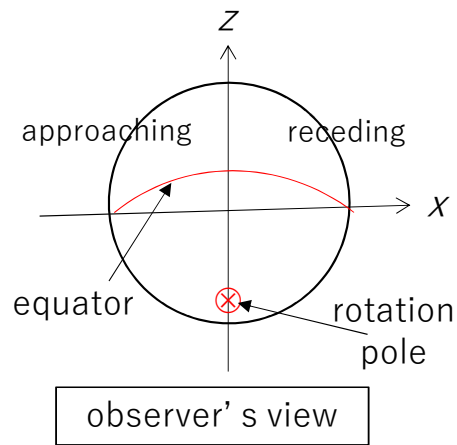
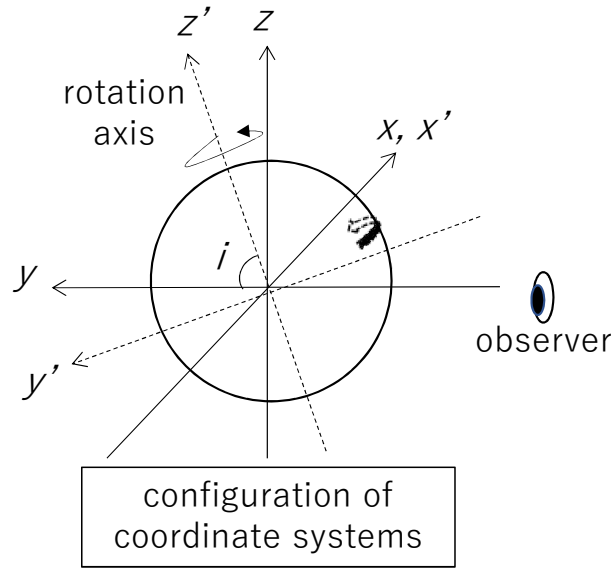


**Fig. 1.** Upper figure: Schematic description of two coordinate systems  $(x, y, z)$  and  $(x', y', z')$ , where the latter is rotated by an angle of  $90^\circ - i$  ( $i$  is the inclination angle of rotation) relative to the former (around the common  $x$ - and  $x'$ -axis) so that the  $y$ -axis matches the observer's line of sight and the  $z'$ -axis coincides with the rotational axis. Lower figure: Observer's view of the stellar disk, which is the projection of the stellar sphere onto the  $x$ - $z$  plane.

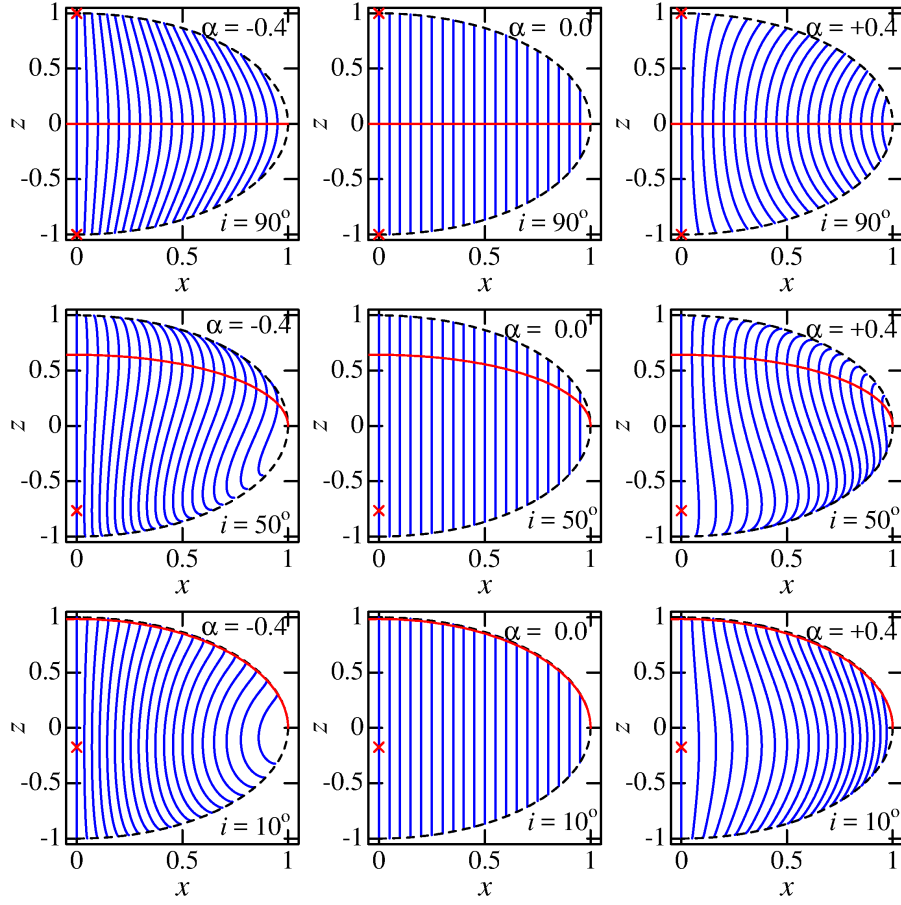


**Fig. 2.** Contours of iso-velocity (i.e., constant radial velocity) on the stellar disk corresponding to  $k = 0.00, 0.05, 0.10, \dots, 0.90, 0.95$ , where  $k (\equiv v/v_e \sin i)$  is the non-dimensional parameter, computed for representative combinations of  $\alpha$  and  $i$ . The left, center, and right panels are for  $\alpha = -0.4, 0.0$ , and  $+0.4$ , while the top, middle, and bottom panels are for  $i = 90^\circ, 50^\circ$ , and  $10^\circ$ , respectively. Also indicated are the equator (red line) and the rotation pole (red cross) visible on the disk.

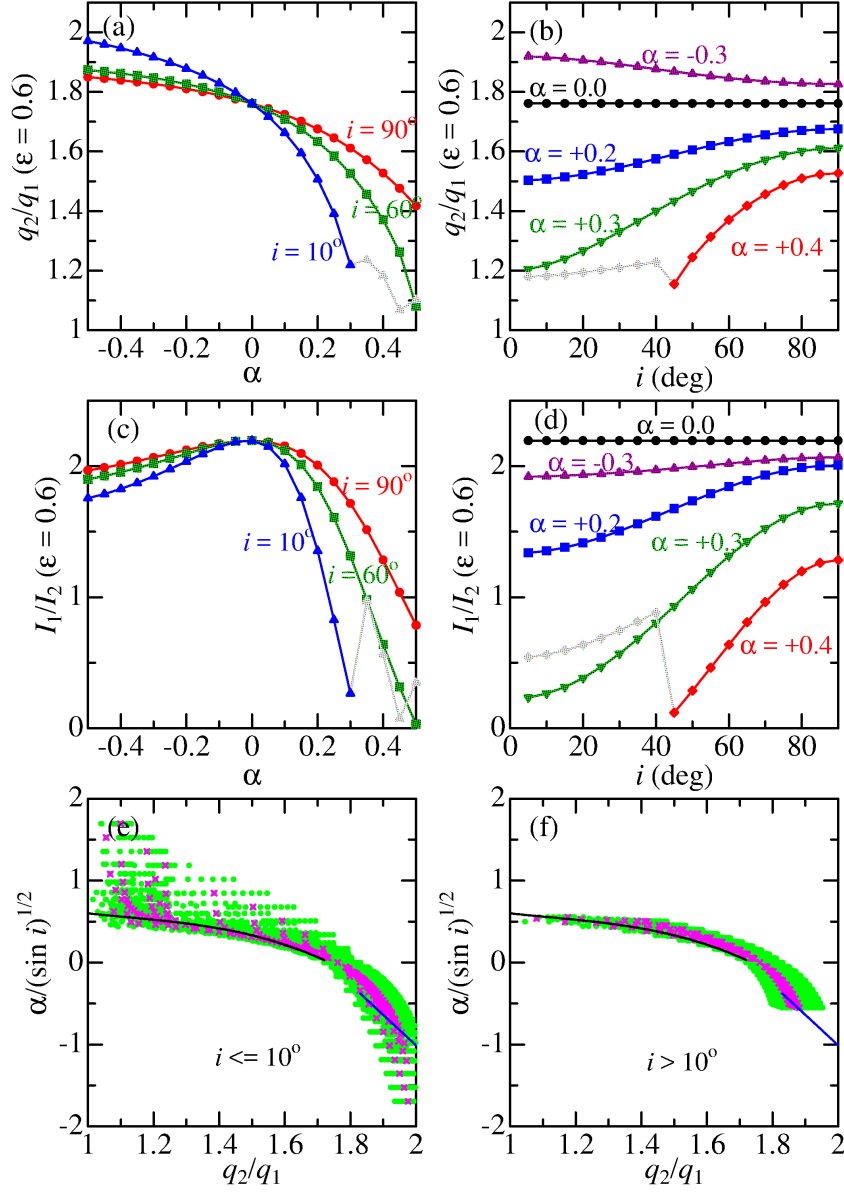


**Fig. 3.** In the upper panels are plotted the  $q_2/q_1$  values (second-to-first zero frequency ratio) against (a)  $\alpha$  and (b)  $i$ , while the middle panels (c) and (d) similarly show the runs of  $I_1/I_2$  (first-to-second sidelobe height ratio), which correspond to the limb-darkening coefficient of  $\epsilon = 0.6$  and are to be compared with Reiners and Schmitt's (2002) Fig. 5 and Fig. 7. Note that the discontinuous phenomena seen for the case of high  $\alpha$  and low  $i$  (obscured in gray) are due to the fact that the first zero in the expected position is no more detected (and thus the "to-be" second zero is in turn regarded as the first zero). The  $\alpha/\sqrt{\sin i}$  vs.  $q_2/q_1$  relations are illustrated in the lower panels (e) (for  $i \leq 10^\circ$ ) and (f) (for  $i > 10^\circ$ ), where all data and those only for  $\epsilon = 0.6$  are depicted by filled circles and crosses, respectively, which should be compared with Fig. 11 of Reiners and Schmitt (2003) [the solid line shows the analytical relation represented by equations (5) and (6) of their paper].

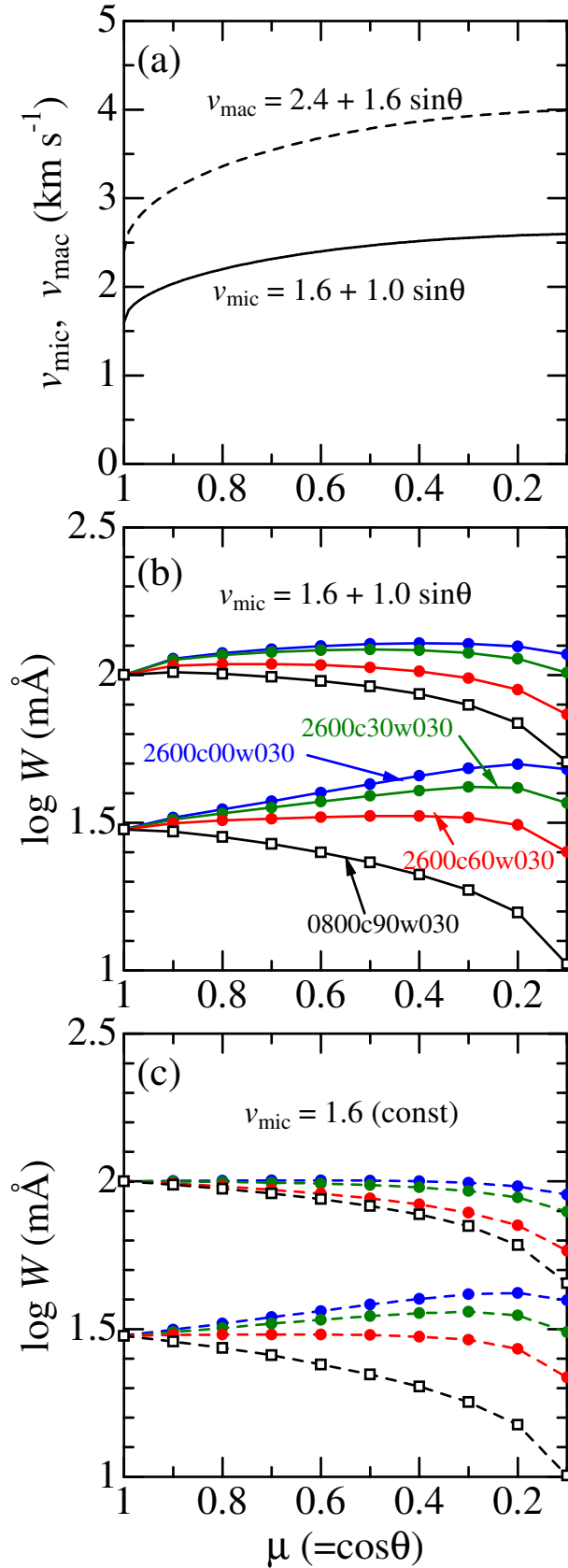


**Fig. 4.** (a) Adopted  $v_{\text{mic}}(\theta)$  (microturbulence given by equation (13); solid line) and  $v_{\text{mac}}(\theta)$  (macroturbulence given by equation (11); dashed line) plotted against  $\mu (\equiv \cos\theta)$ . (b) Angle-dependence of the equivalent widths ( $W$ ) computed by using  $v_{\text{mic}}(\theta)$  of equation (13) for 8 fictitious lines. (Note that the line data listed in table 1 are arranged in the same order as the curves in this figure.) (c) Angle-dependence of the equivalent widths ( $W$ ) for 8 fictitious lines similar to (b), but computed by using the constant  $v_{\text{mic}}$  of  $1.6 \text{ km s}^{-1}$

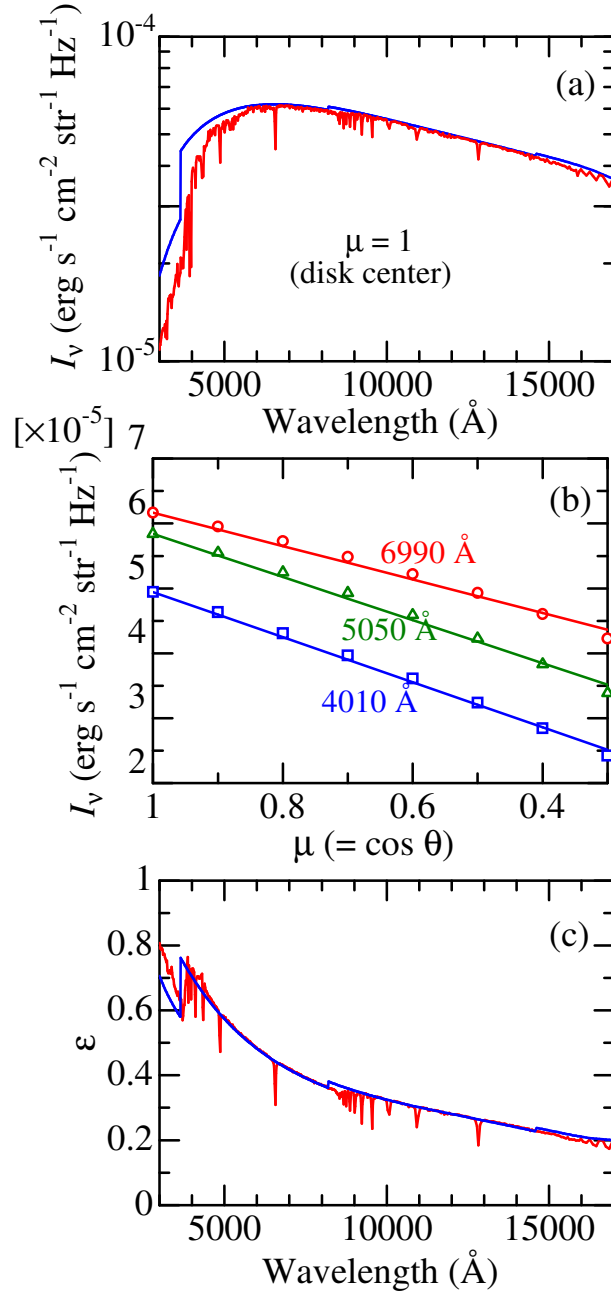


**Fig. 5.** (a) Energy distribution of the specific intensity ( $I_\nu$ ) at the line center ( $\mu = \cos\theta = 1$ ) computed from the atmospheric model ( $T_{\text{eff}} = 6500$  K,  $\log g = 4.29$ , solar abundance) adopted in this study, where the line-included and pure-continuum distributions are depicted in red and blue lines, respectively. (b) Angle-dependence of continuum  $I(\nu)$  at 4010 Å, 5050 Å, and 6990 Å (symbols) along with the linear-regression lines derived from these data between  $\mu = 1$  and 0.3 (lines). (c) Wavelength-dependence of  $\epsilon$  (limb-darkening coefficient) defined as the slope of the linear-regression line such like as in panel (b). As in panel (a), the red and blue lines correspond to the cases of line-included intensity and pure-continuum intensity, respectively.

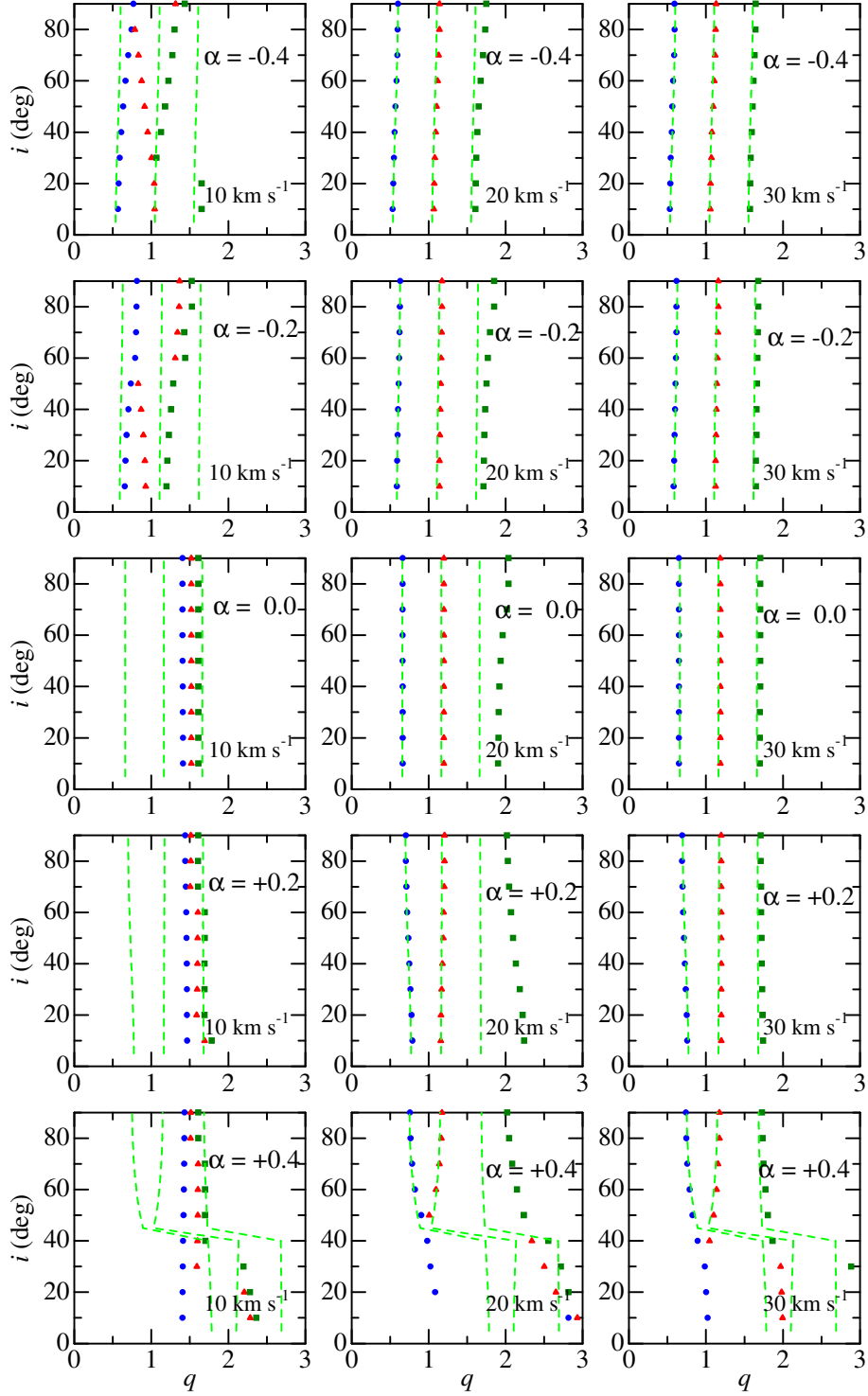


**Fig. 6.** Graphical display showing how the first-, second-, and third-zero frequencies (depicted by circles, triangles, and squares, respectively) computed for the 2600c30w100 line behave with a change in  $i$  (inclination angle) for different cases of  $\alpha$  and  $v_e \sin i$ . Note that the non-dimensional frequency  $q$  [cf. equation (14)] is used in the abscissa instead of the actual  $\sigma$  ( $\text{\AA}^{-1}$ ), in order to enable a direct comparison irrespective of  $v_e \sin i$ . The zero positions expected for the standard rotational broadening function ( $\epsilon = 0.6$ ; cf. subsection 4.1) are shown by dashed lines. The panels in the first, second, third, fourth, and fifth row correspond to  $\alpha = -0.4, -0.2, 0.0, +0.2,$  and  $+0.4$ , while those in the left, center, and right column are for  $v_e \sin i = 10, 20,$  and  $30 \text{ km s}^{-1}$ , respectively.

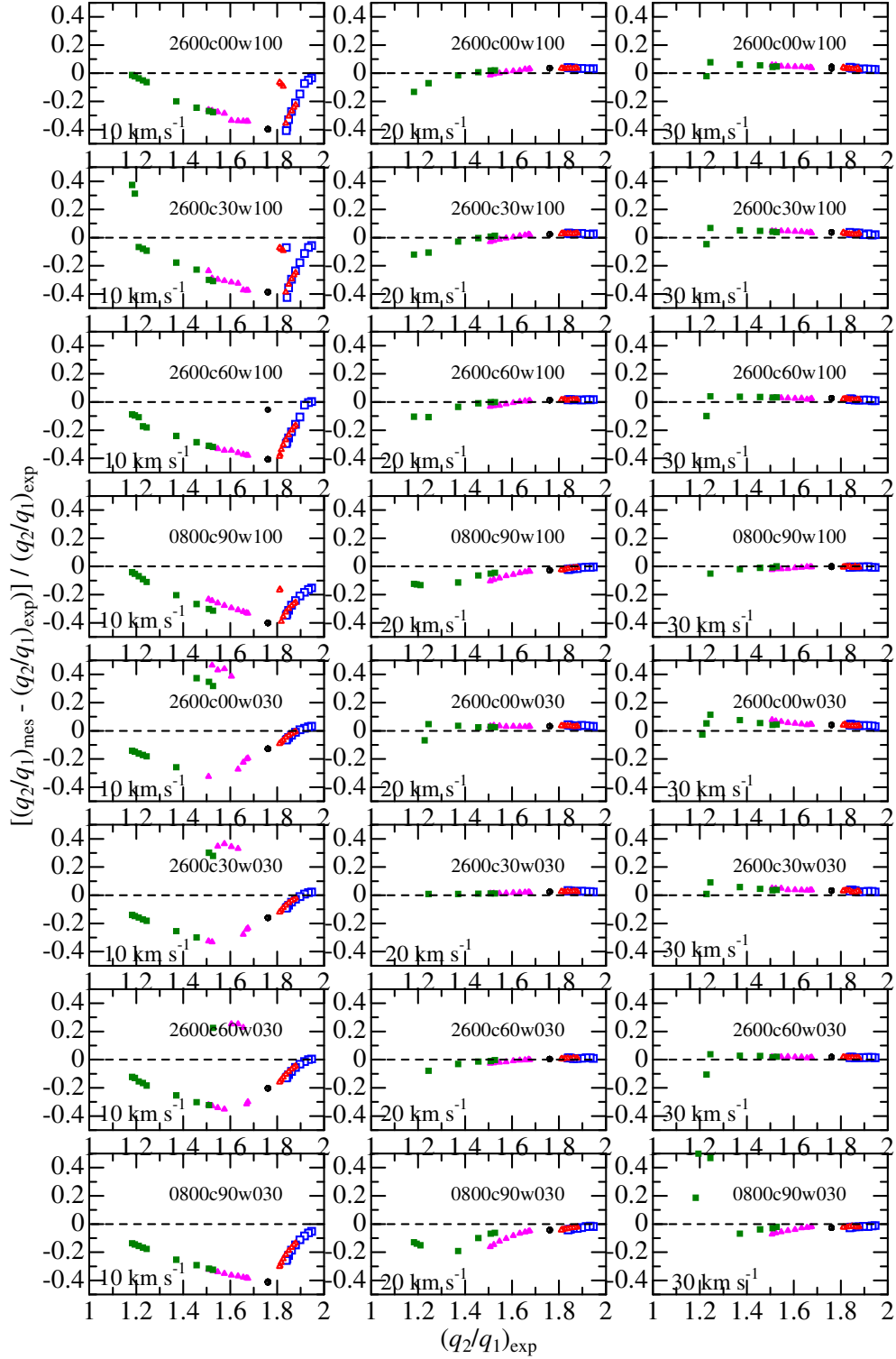


**Fig. 7.** Diagrams showing how the measured second-to-first zero frequency ratios  $[(q_2/q_1)_{\text{mes}}]$  deviate from the expected values from the standard rotational broadening function  $[(q_2/q_1)_{\text{exp}}]$ ; corresponding to  $\epsilon = 0.6$ , computed for the eight lines presented in table 1 (note that the panels in each of the eight rows are arranged in the same order as in the table). The left, middle, and right panels are for  $v_e \sin i = 10, 20,$  and  $30 \text{ km s}^{-1}$ , respectively. The results (for nine  $i$  values from  $10^\circ$  to  $90^\circ$ ) for each of the five different  $\alpha$  values are shown here, which are discriminated by the symbols:  $\alpha = -0.4$  (open squares),  $-0.2$  (open triangles),  $0.0$  (half-filled circles),  $+0.2$  (filled triangles), and  $+0.4$  (filled squares).

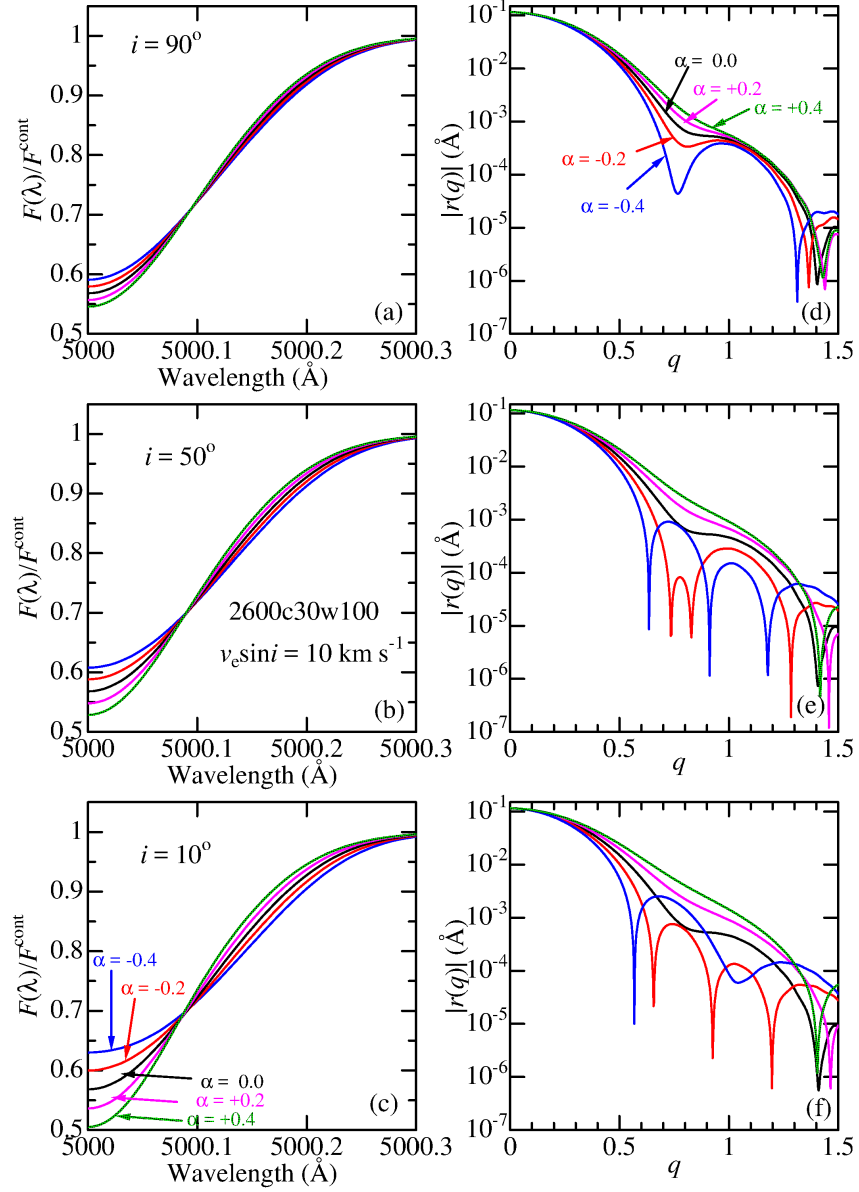


**Fig. 8.** The left panels display the residual fluxes  $[F(\lambda)/F^{\text{cont}}]$  of the 2600c30w100 line simulated with the specified  $v_e \sin i$  of  $10 \text{ km s}^{-1}$  for the five values of  $\alpha$  ( $-0.4$ ,  $-0.2$ ,  $0.0$ ,  $+0.2$ , and  $+0.4$ ), while the right panels show the corresponding Fourier transform amplitudes  $|r(q)|$  of the line depth  $[R(\lambda) \equiv 1 - F(\lambda)/F^{\text{cont}}]$  (where non-dimensional  $q$  is used as abscissa such as like in figure 6): (a, d)  $i = 90^\circ$ , (b, e)  $i = 50^\circ$ , and (c, f)  $i = 10^\circ$ .

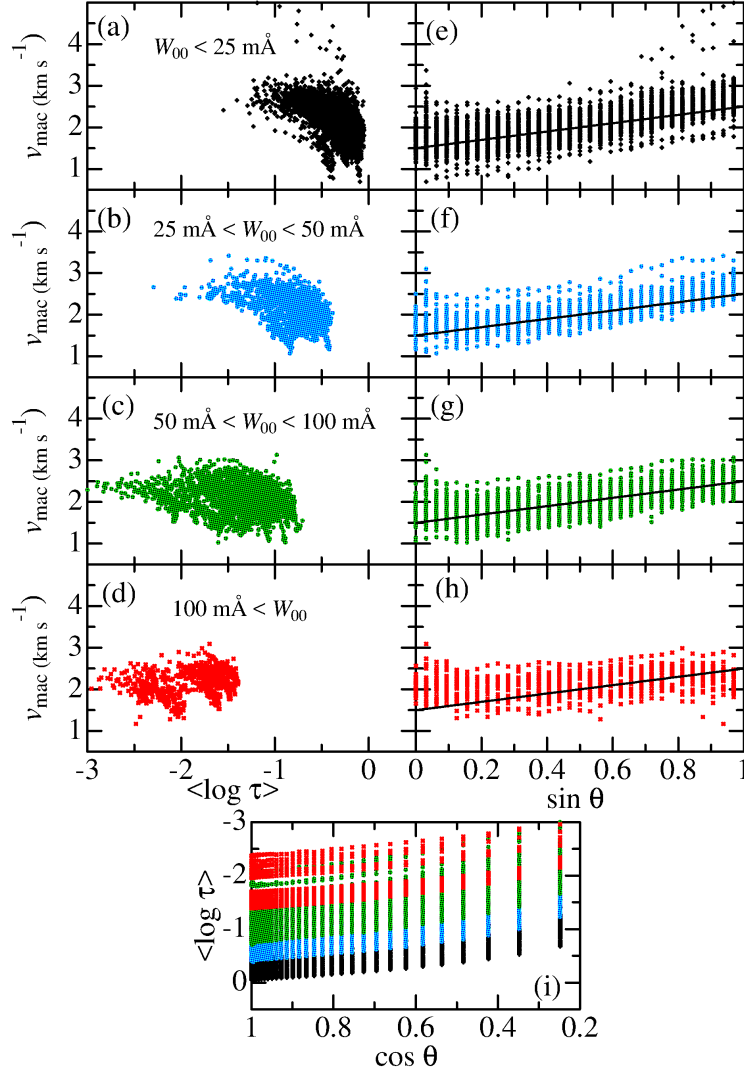


**Fig. 9.** The  $v_{\text{mac}}$  values (line-of-sight velocity dispersion of Gaussian macroturbulence) at each point of the solar disk, which were derived by Takeda and UeNo (2019) for 280 Fe I lines, are plotted against  $\langle \log \tau \rangle$  (mean formation depth; left panels (a)–(d)) and  $\sin \theta$  (right panels (e)–(h)), where the data in each panel are grouped according to the range of disk-center equivalent width ( $W_{00}$ ). (a),(e):  $W_{00} < 25 \text{ m\AA}$  (black symbols), (b),(f):  $25 \text{ m\AA} \leq W_{00} < 50 \text{ m\AA}$  (blue symbols), (c),(g):  $50 \text{ m\AA} \leq W_{00} < 100 \text{ m\AA}$  (green symbols), and (d),(h):  $100 \text{ m\AA} \leq W_{00}$  (red symbols). The adopted mean relation,  $v_{\text{mac}} = 1.5 + 1.0 \sin \theta$  (cf. equation (10)), is drawn by solid lines in each of the right panels (e)–(h). The bottom panel (i) shows the correlation between  $\langle \log \tau \rangle$  and  $\cos \theta$  (all data overplotted).

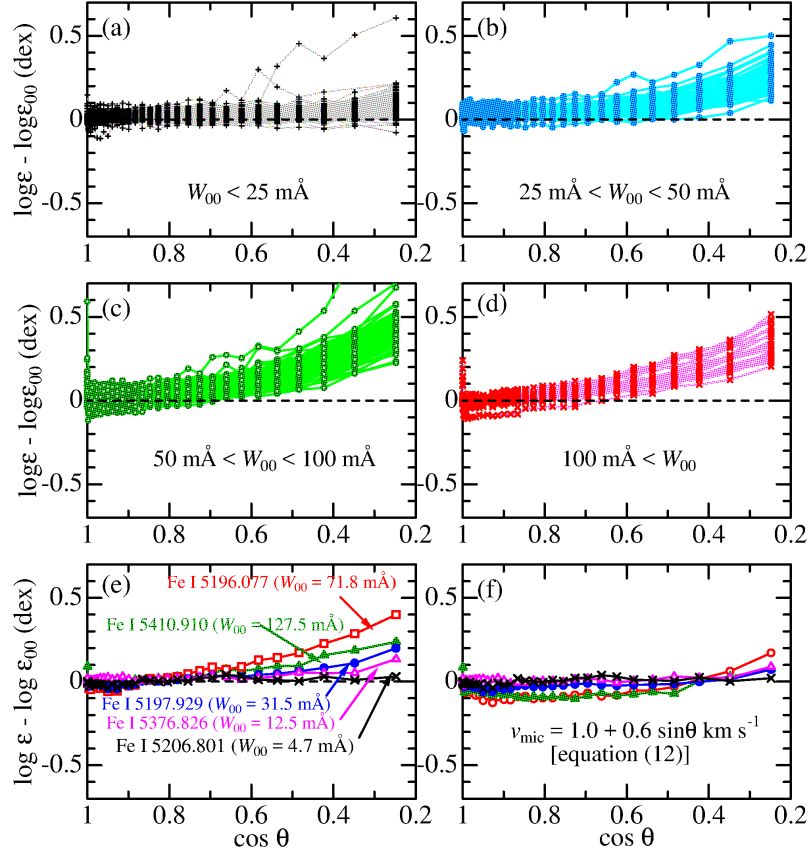


**Fig. 10.** Differences of abundances relative to the disk center-value ( $\log \epsilon - \log \epsilon_{00}$ ), which were derived based on the solar center-limb equivalent widths ( $W$ ) of 280 Fe I lines published by Takeda and UeNo (2019) by assuming a constant microturbulence of  $v_{\text{mic}} = 1 \text{ km s}^{-1}$  (except for panel (f)), are plotted against  $\cos \theta$ , where each of panels (a), (b), (c), and (d) correspond to different four line-strength classes as in figure 9 (with the same colors). The results for five representative lines of different strengths are shown in the bottom panels (e) and (f), each corresponding to  $v_{\text{mic}} = 1 \text{ km s}^{-1}$  and angle dependent  $v_{\text{mic}} = 1.0 + 0.6 \sin \theta \text{ km s}^{-1}$  given by equation (12)), respectively: Fe I 5206.801 ( $W_{00} = 4.7 \text{ mÅ}$ ), Fe I 5376.826 ( $W_{00} = 12.5 \text{ mÅ}$ ), Fe I 5197.929 ( $W_{00} = 31.5 \text{ mÅ}$ ), Fe I 5196.077 ( $W_{00} = 71.8 \text{ mÅ}$ ), and Fe I 5410.910 ( $W_{00} = 127.5 \text{ mÅ}$ ).

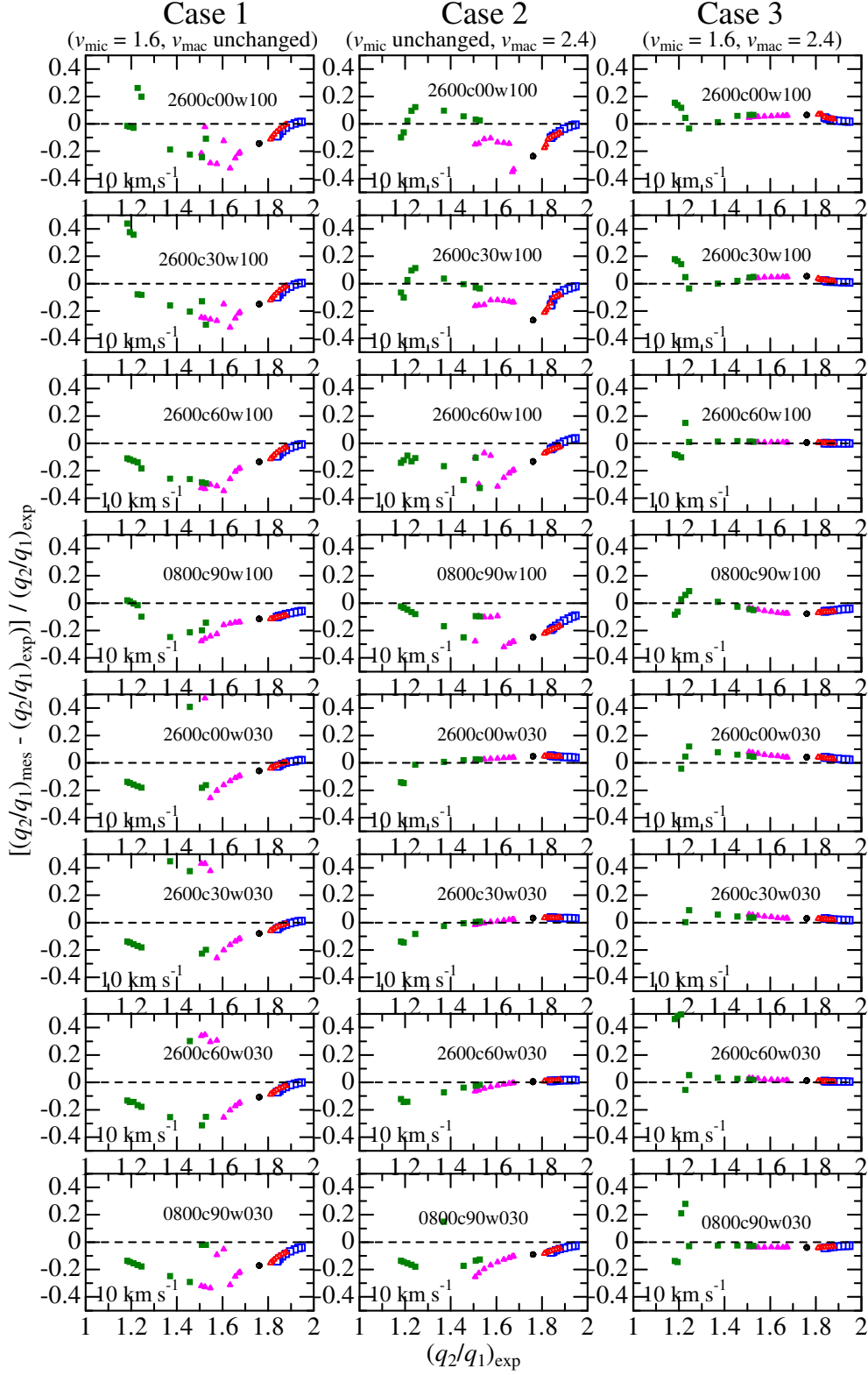


**Fig. 11.** Results of test calculations showing how the serious deviations of measured  $(q_2/q_1)_{\text{mes}}$  from the expected  $(q_2/q_1)_{\text{exp}}$  for the  $v_e \sin i = 10 \text{ km s}^{-1}$  cases are changed by using the simple constant  $v_{\text{mac}}$  ( $2.4 \text{ km s}^{-1}$ ) or  $v_{\text{mic}}$  ( $1.6 \text{ km s}^{-1}$ ) instead of the standard  $\theta$ -dependent relations [cf. equations (11) and (13)]. Left panels — Case 1 ( $v_{\text{mac}}(\theta)$  unchanged while  $v_{\text{mic}} = 1.6 \text{ km s}^{-1}$ ). Middle panels — Case 2 ( $v_{\text{mac}} = 2.4 \text{ km s}^{-1}$  while  $v_{\text{mic}}(\theta)$  unchanged). Right panels — Case 3 ( $v_{\text{mac}} = 2.4 \text{ km s}^{-1}$  and  $v_{\text{mic}} = 1.6 \text{ km s}^{-1}$ ). These figures panels are so arranged as to be directly comparable with the left-hand panels of figure 7 ( $v_e \sin i = 10 \text{ km s}^{-1}$  case, corresponding to the standard  $v_{\text{mic}}(\theta)$  and  $v_{\text{mac}}(\theta)$ ); see the caption therein for more details.